Check for updates

How to cite: *Angew. Chem. Int. Ed.* **2023,** *62,* e202211361
International Edition: doi.org/10.1002/anie.202211361
German Edition: doi.org/10.1002/ange.202211361

Iron Chemistry

Characterization of a Ferryl Flip in Electronically Tuned Nonheme Complexes. Consequences in Hydrogen Atom Transfer Reactivity

Valeria Dantignana[+], M. Carmen Pérez-Segura[+], Pau Besalú-Sala, Estefanía Delgado-Pinar, Álvaro Martínez-Camarena, Joan Serrano-Plana, Andrea Álvarez-Núñez, Carmen E. Castillo, Enrique García-España, Josep M. Luis,* Manuel G. Basallote,* Miquel Costas,* and Anna Company**

Abstract: Two oxoiron(IV) isomers (^{R}**2a** and ^{R}**2b**) of general formula $[Fe^{IV}(O)(^{R}PyNMe_3)(CH_3CN)]^{2+}$ are obtained by reaction of their iron(II) precursor with NBu_4IO_4. The two isomers differ in the position of the oxo ligand, *cis* and *trans* to the pyridine donor. The mechanism of isomerization between ^{R}**2a** and ^{R}**2b** has been determined by kinetic and computational analyses uncovering an unprecedented path for interconversion of geometrical oxoiron(IV) isomers. The activity of the two oxoiron(IV) isomers in hydrogen atom transfer (HAT) reactions shows that ^{R}**2a** reacts one order of magnitude faster than ^{R}**2b**, which is explained by a repulsive noncovalent interaction between the ligand and the substrate in ^{R}**2b**. Interestingly, the electronic properties of the R substituent in the ligand pyridine ring do not have a significant effect on reaction rates. Overall, the intrinsic structural aspects of each isomer define their relative HAT reactivity, overcoming changes in electronic properties of the ligand.

[*] V. Dantignana,[+] P. Besalú-Sala, J. Serrano-Plana, A. Álvarez-Núñez, J. M. Luis, M. Costas, A. Company
Institut de Química Computacional i Catàlisi (IQCC), Departament de Química, Universitat de Girona
C/Mª Aurèlia Capmany 69, 17003 Girona, Catalonia (Spain)
E-mail: josepm.luis@udg.edu
miquel.costas@udg.edu
anna.company@udg.edu

M. C. Pérez-Segura,[+] C. E. Castillo, M. G. Basallote
Departamento de Ciencia de los Materiales e Ingeniería Metalúrgica y Química Inorgánica, Facultad de Ciencias, Instituto de Biomoléculas (INBIO), Universidad de Cádiz
Puerto Real, 11510 Cádiz (Spain)
E-mail: manuel.basallote@uca.es

E. Delgado-Pinar, Á. Martínez-Camarena, E. García-España
Departamento de Química Inorgánica, Instituto de Ciencia Molecular (ICMol), Universidad de Valencia
C/Catedrático José Beltrán, Paterna, 46980 Valencia 2 (Spain)
E-mail: enrique.garcia-es@uv.es

[+] These authors contributed equally to this work.

© 2022 The Authors. Angewandte Chemie International Edition published by Wiley-VCH GmbH. This is an open access article under the terms of the Creative Commons Attribution Non-Commercial NoDerivs License, which permits use and distribution in any medium, provided the original work is properly cited, the use is non-commercial and no modifications or adaptations are made.

Introduction

Oxoiron(IV) compounds have been identified as the active oxidants involved in the catalytic cycle of several nonheme iron-dependent oxygen activation enzymes.[1] A common structural feature of these oxoiron(IV) species is the presence of two non-equivalent *cis*-labile sites at the iron center, which renders the possibility of the existence of two geometrical isomers.[2,3] This is in stark contrast with heme sites, where the porphyrin leaves two *trans* axial positions available.[4] The significance of the existence of geometrical isomers is often disregarded, and may be quite challenging to address because they are expected to have similar spectroscopic properties. Furthermore, isomerization between geometrical oxoiron(IV) isomers, a process known as "ferryl flip", has been proposed to take place in the reaction mechanism of several α-ketoglutarate dependent dioxygenases such as clavaminate synthase[5] and DNA-repairing AlkB oxygenases.[6] In these cases, isomerization places the reactive oxo group in the proper position for reaction with the substrate.

Exceptionally, Mössbauer spectroscopic studies on nonheme iron dependent halogenases SyrB2 and CytC3 revealed the presence of two interconverting oxoiron(IV)-chloride intermediates directly involved in the aliphatic halogenation of the substrate,[7,8] which may correspond to structural isomers according to DFT calculations.[9] Overall, geometrical isomery may be an important aspect defining the reactivity of nonheme oxoiron(IV) species.

Small molecule model complexes may offer a tool to investigate how subtle aspects of the coordination structure of oxoiron(IV) species affect their chemistry.[10–14] Examples of oxoiron(IV) complexes that could exist as different geometrical isomers are exceedingly rare,[15–17] and isomerization mechanisms are poorly understood, an aspect that also applies to enzymatic sites.

Judicious ligand design in coordination complexes can also help to clarify the effect of crystal field (energy difference between spin states), sterics and electronics in defining the oxidation abilities of oxoiron(IV) complexes. Several studies have addressed the first two aspects in a quite systematic manner.[18–27] On the contrary, studies describing systematic tuning of the ligand electronic properties of the oxoiron(IV), without modifying sterics, are rather scarce and limited to pentadentate ligands.[28]

 © 2022 The Authors. Angewandte Chemie International Edition published by Wiley-VCH GmbH

We have recently reported oxoiron(IV) species bearing a tetradentate N-based ligand, $[Fe^{IV}(O)(^{H}PyNMe_3)(CH_3CN)]^{2+}$ (^{H}**2**), formed as a 1:1 mixture of two geometrical isomers (Figure 1).[29] Over time, the less stable isomer (^{H}**2a**) converts into the thermodynamically most stable one (^{H}**2b**). The two isomers differ also in their reactivity: ^{H}**2a** reacts roughly one order of magnitude faster than ^{H}**2b** in hydrogen atom transfer (HAT), but it is slightly less reactive in oxygen atom transfer (OAT). This further supports the idea that the position of the oxo group in the coordination sphere of the iron center is important to dictate the reactivity.

In this work this concept is substantiated and generalized for a family of iron(II) complexes $[Fe^{II}(CF_3SO_3)_2(^{R}PyNMe_3)]$ (^{R}**1**) supported by electronically-tuned $^{R}PyNMe_3$ ligands (R = MeO, Cl, Br, CO_2Me, CF_3, Figure 1). The isomerization of the corresponding oxoiron(IV) compounds (^{R}**2**) has been studied by kinetic and computational methods, putting forward a novel mechanism that may serve as a model for the enzymatic "ferryl flip". Furthermore, this series of complexes constitutes a unique platform to evaluate the impact of both the position of the oxo group and electronics on the reactivity of oxoiron(IV) compounds. By doing so, the study reveals unexpected trends, whose detailed analysis provides insight into the nature of HAT and OAT reactions.

Results and Discussion

Synthesis of Ligands and Iron(II) Complexes

The new ligands include the electron-rich $^{MeO}PyNMe_3$ and the electron-poor $^{Cl}PyNMe_3$, $^{Br}PyNMe_3$ $^{CO2Me}PyNMe_3$ and $^{CF3}PyNMe_3$ so that the impact of the electron-donating abilities of the pyridine group of the ligand on the reactivity of the oxoiron(IV) species can be evaluated. $[Fe^{II}(CF_3SO_3)_2(^{R}PyNMe_3)]$ complexes (^{R}**1**) were prepared by reaction of the corresponding ligand with equimolar amounts of $[Fe^{II}(CF_3SO_3)_2(CH_3CN)_2]$ (see Supporting Information for details) and obtained as crystalline materials.

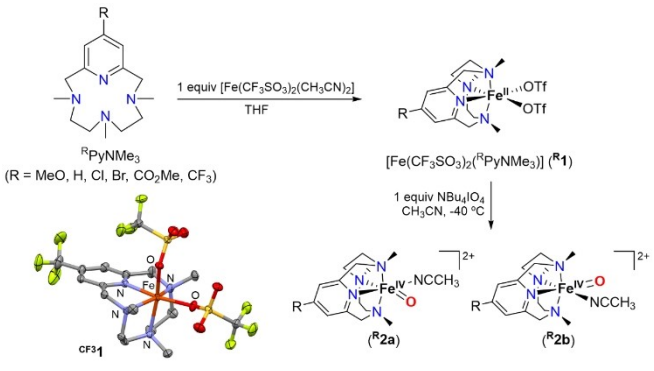

Figure 1. Structures of $^{R}PyNMe_3$ ligands, iron(II) complexes (^{R}**1**) and oxoiron(IV) compounds (^{R}**2a** and ^{R}**2b**) along with the thermal ellipsoid plot (50% probability) for ^{CF3}**1** (hydrogen atoms have been omitted for clarity).

Complexes ^{R}**1** were all characterized in the solid state by single crystal X-ray diffraction (Figure 1 and S72–S75, the structures for ^{H}**1** and ^{MeO}**1** have been previously reported).[30–32] In all cases, the complexes adopt distorted octahedral geometries in which the four nitrogen atoms of the ligands are bonded to the iron(II) center. The coordination sphere is completed by triflate ligands disposed in a relative *cis* configuration. The average Fe–N distance of 2.2 Å is characteristic of a high spin state of the iron center.[33,34] Interestingly, the spin state was maintained in solution, as ascertained by ^{1}H NMR spectroscopy, which shows broad signals and large spectral windows ranging from approximately −40 to 140 ppm (Figure S77). Moreover, effective magnetic moments (μ_{eff}) measured using the Evans' method range from 4.9 to 5.2 μ_B for ^{R}**1** (Table S1 and Figure S71), further confirming a major contribution of the S = 2 spin state. Finally, cyclic voltammetry of ^{R}**1** indicated that the γ substituent has a direct impact on the redox potential of the Fe^{III}/Fe^{II} pair (Figure 2). As expected,[35] the redox potential increases when the electrondonating properties of the substituent decreases, so that the $E_{1/2}$ values directly correlate with the Hammett parameter. Thus, ^{MeO}**1** shows the lowest redox potential (0.66 V vs $Ag/AgNO_3$) and ^{CF3}**1** the largest (0.81 V vs $Ag/AgNO_3$).

Kinetics of the Formation and Isomerization of the Oxoiron(IV) Species

As previously reported for ^{H}**1**,[29] reaction of ^{R}**1** with stoichiometric amounts of NBu_4IO_4 in acetonitrile at −35 °C affords the corresponding oxoiron(IV) species. Thus, upon

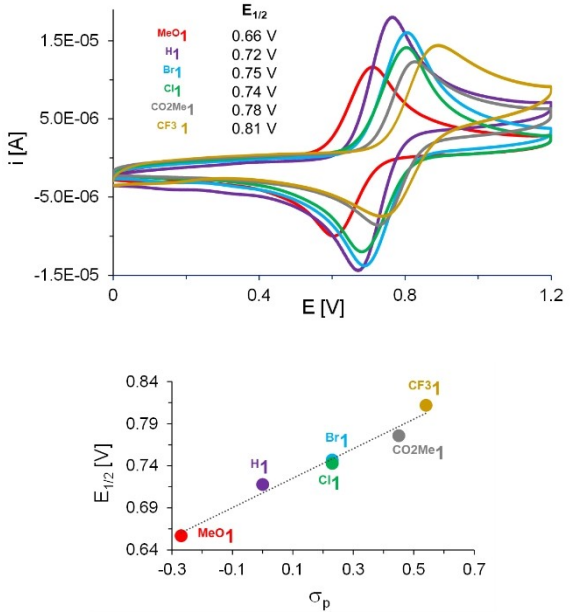

Figure 2. Top: Cyclic voltammetries of ^{R}**1** (1 mM) recorded in acetonitrile vs $Ag/AgNO_3$ at 298 K (Supporting electrolyte: Bu_4NPF_6 0.1 M). Bottom: Correlation of the redox potential with the Hammett parameter (σ_p).

© 2022 The Authors. Angewandte Chemie International Edition published by Wiley-VCH GmbH

15213773, 2023, 2, Downloaded from https://onlinelibrary.wiley.com/doi/10.1002/anie.202211361 by Universidad De Cadiz, Wiley Online Library on [28/09/2023]. See the Terms and Conditions (https://onlinelibrary.wiley.com/terms-and-conditions) on Wiley Online Library for rules of use; OA articles are governed by the applicable Creative Commons License

oxidant addition the characteristic UV/Vis features of ^{R}**1** disappear concomitant with the formation of two low intensity absorption bands at ≈800 nm and ≈1000 nm characteristic of ^{R}**2**. This process is so rapid that no detailed analysis on the formation of ^{R}**2** could be made. Interestingly, for all the complexes the relative intensity of the two bands changes over time (Figure 3 and Figure S85). Thus, the intensity of the band at 800 nm decreases with coincident increase of the 1000 nm band and an isosbestic point at ≈940 nm appears along this process. By analogy with ^{H}**2**, these two bands are assigned to two different geometrical oxoiron(IV) isomers whose spectra differ in the relative intensities of both bands. The only structural difference between the two isomers is the position of the oxo and acetonitrile ligands and thus, the process observed by UV/Vis spectroscopy corresponds to the isomerization of one isomer (^{R}**2a**) into the other (^{R}**2b**) which are initially formed in a c.a. 1:1 mixture. Albeit previous studies with ^{H}**2** were carried out in the presence of triflic acid,[29] preliminary experiments showed that addition of small amounts of this acid only led to minor changes in the rate of isomerization, and so all kinetic experiments in the present work were carried out in the absence of acid.

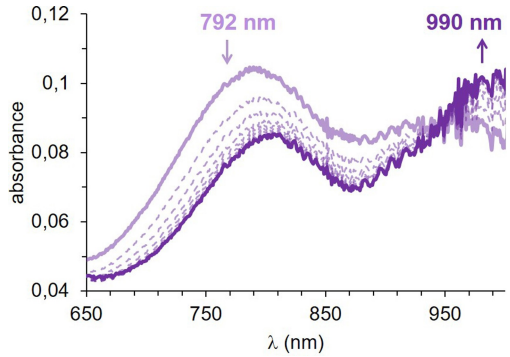

Figure 3. Typical spectral changes observed upon reaction of ^{H}**1** (1 mM) with 1 equiv NBu_4IO_4 in acetonitrile at −30 °C. Only the isomerization phase is shown. The initial phase of the reaction accounting for the fast formation of a 1:1 mixture of ^{H}**2a**:^{H}**2b** is not shown.

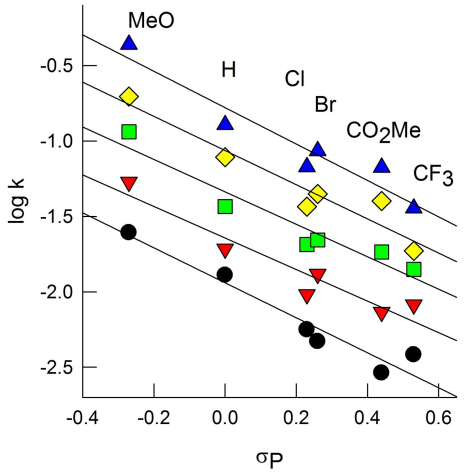

Figure 4. Hammett plot for the isomerization of ^{R}**2a** into ^{R}**2b** complexes: −40 °C (black), −35 °C (red), −30 °C (green), −25 °C (yellow) and −20 °C (blue).

The spectral changes corresponding to the isomerization of ^{R}**2a** into ^{R}**2b** could be fitted to a single exponential. Experiments at different temperatures were carried out to derive the corresponding activation parameters using the Eyring equation (Table 1). Although in some cases the occurrence of a slower step for the self-decay of ^{R}**2b** is evident, this process was not analyzed in detail because it usually exceeded the stopped-flow time scale. The values in Table 1 clearly show that the nature of R causes significant changes in the isomerization rate constants and the activation parameters. The rate constants increase when the donor character of the R substituent increases, and Hammett plots at the different temperatures (Figure 4) show negative slopes within the narrow −1.1 to −1.2 range, the mean value for all temperatures being of −1.13(6). This negative slope indicates that some positive charge is built at the complex during the isomerization process, which can be considered to result from total or partial dissociation of an acetonitrile ligand. The small values of the activation entropy and the independence of the isomerization rate constant with the acetonitrile concentration in acetone-acetonitrile mixtures (Table S12 and Figure S87) suggest a novel mechanism involving acetonitrile exchange between two different coordination sites in the oxoiron(IV) species. In an effort to further understand the mechanism of the isomerization, the process was monitored by CSI-MS (Cold-Spray Ionization Mass Spectrometry) in the presence of $H_2{}^{18}O$, but no ^{18}O-incorporation into the oxoiron(IV) species was observed along the reaction (Figure S84). This indicates that a putative oxo-hydroxo tautomerism reminiscent of the processes described for previously reported heme and non-heme systems[17,36–38] is not occurring in this case and water is not directly involved in the conversion of ^{R}**2a** into ^{R}**2b**.

The activation parameters in Table 1 show a good isokinetic relationship (Figure S89) but the ordering of the different complexes differs from that of the Hammett parameters. A more detailed analysis (see section 5.2 in the Supporting Information) reveals that the correlation is mainly caused by compensation of errors due to the correlation between the estimates of $\Delta H^{\neq}$ and $\Delta S^{\neq}$. Unbiased estimates of the activation parameters ($\Delta H^{\neq}$ and $\Delta G^{\neq}$) were obtained by evaluating the Arrhenius equation at the harmonic mean temperature (T_{hm}) and the values of $\Delta G^{\neq}$ at T_{hm} are also included in Table 1. The $\Delta G^{\neq}$ values are obtained with more precision than the Eyring activation parameters and show a linear dependence with respect to σ_P with a slope similar in absolute value to that in the Hammett plot, thus showing that Hammett plots using the experimental rate constants have superior capability to analyze the effect of substituents on the isomerization process than using activation parameters derived from the Eyring equation. In any case, the present results clearly support an isomerization mechanism for the ^{R}**2** species that involves acetonitrile exchange between two different coordination sites through a predominantly dissociative interchange mechanism, which

© 2022 The Authors. Angewandte Chemie International Edition published by Wiley-VCH GmbH

15213773, 2023, 2, Downloaded from https://onlinelibrary.wiley.com/doi/10.1002/anie.202211361 by Universidad De Cadiz, Wiley Online Library on [28/09/2023]. See the Terms and Conditions (https://onlinelibrary.wiley.com/terms-and-conditions) on Wiley Online Library for rules of use; OA articles are governed by the applicable Creative Commons License

Table 1: Summary of kinetic data and activation parameters for the isomerization of ^{R}**2a** into ^{R}**2b** in acetonitrile solution.

R	k_{isom}[a] [s^{-1}]	$\Delta H^{\neq}$ [kcal mol^{-1}]	$\Delta S^{\neq}$ [cal K^{-1} mol^{-1}]	$\Delta G_{243}{}^{\neq}$[b] [kcal mol^{-1}]	$\Delta G_{243}{}^{\neq}$[c] [kcal mol^{-1}]
MeO	0.0535(6)	16.1(5)	3(2)	15.21(1)	15.20
H	0.0193(2)	13.5(9)	−9(3)	15.69(2)	15.75
Cl	0.00961(4)	14.3(4)	−7(2)	16.03(1)	16.03
Br	0.0131(1)	16.1(9)	0(4)	15.97(2)	15.99
CO_2Me	0.00735(5)	18.2(9)	9(4)	16.12(3)	16.08
CF_3	0.00822(6)	12.0(9)	−18(4)	16.24(3)	16.21

[a] Measured at −35 °C. [b] Results obtained by fitting to the Arrhenius equation at the mean harmonic temperature (T_{hm} = 243 K). [c] Value derived from the rate constant at −30 °C. The estimation of the errors is in all cases smaller than 0.01. Note that T_{hm} (harmonic mean) is slightly lower than the mean temperature (242.95 K vs. 243.15 K).

causes a decrease of the electron density at the metal complex that is better accommodated when the ligand contains donor substituents. The magnitude of this effect is up to 1 kcal mol^{-1} in the $\Delta G^{\neq}$ values that translates to about one order of magnitude in the rate constants.

Computational Analysis of the Isomerization Mechanism

The isomerization mechanism for ^{H}**2**, ^{MeO}**2** and ^{CF3}**2** was modelled in silico for both S = 1 and S = 2 spin states (see computational details in the Supporting Information). The chosen DFT functional (M06 L) correctly predicts that isomer ^{H}**2b** is slightly more stable than ^{H}**2a**, which is also in agreement with highly accurate *ab initio* DLPNO-CCSD(T) results (Table S13). For species ^{R}**2a** and ^{R}**2b**, S = 1 and S = 2 spin states are close in energy. This is also true when B3LYP and ωB97XD functionals are used (Table S13). However, if only the electronic energy is considered, S = 1 states are always the most stable ones for all studied functionals and DLPNO-CCSD(T) *ab initio* method. On the contrary, the proposed transition states (^{R}**TS$_{isom}$**, see below) are clearly better described as S = 2. The DFT Gibbs energy barriers for the isomerization process are 20.4 (^{MeO}**2**), 21.0 (^{H}**2**) and 22.0 (^{CF3}**2**) kcal mol^{-1} (Figure 5). Thus, the DFT barriers reproduce the decrease of the isomerization barrier when the pyridine moiety contains electron-donating groups, in agreement with the Hammett plot (Figure 4). The structure of the transition state corroborates that the isomerization proceeds through a dissociative interchange mechanism, quite similar to that operating for solvent exchange in metal complexes[39,40] but involving attack by the entering acetonitrile at a different coordination site. This process involves dissociation of the initially bound acetonitrile molecule and coordination of another solvent molecule at a relative *cis* position, so that both acetonitrile ligands are weakly bound to the iron center in the TS (i.e. Fe-acetonitrile bond lengths > 3.2 Å) (Figure 5 and Table S16). Furthermore, the charges on the complex and in both acetonitrile molecules computed for ^{R}**2a** and ^{R}**TS$_{isom}$** using the APOST3D program,[41,42] elucidate a positive charge accumulation on the complex of 0.009, 0.014 and 0.025 electrons for R = OMe, R = H and R = CF_3, respectively (Table S14). Such positive charge accumulation is in agreement with the conclusions derived from the Hammett plot

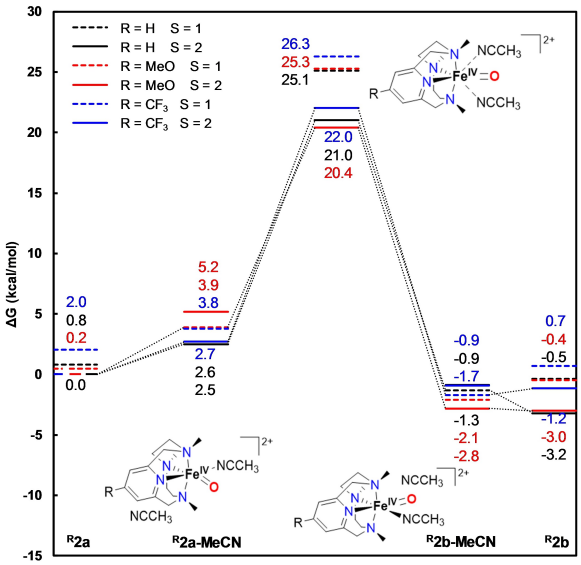

Figure 5. Isomerization energy profile computed at M06L–D3/Def2TZVP/SMD//M06L–D3/Def2SVP/SMD level of theory for R = H (black), OMe (red) and CF_3 (blue) for S = 1 (dashed) and S = 2 (solid) spin states.

and also suggests a predominantly dissociative exchange mechanism for the isomerization.

Other mechanisms for the isomerization were explored by DFT means, as for instance the out-of-plane rotation of the oxo and acetonitrile groups, or the predominantly associative exchange mechanism.[43,44] None of them was energetically accessible since the former requires the loss of the chelate effect of the $PyNMe_3$ ligand, and the latter requires the formation of an unstable heptacoordinate intermediate.

Context and Significance of the Isomerization Mechanism

The mechanisms of geometric isomerization in octahedral coordination complexes have been studied in detail. Examples of geometric rearrangements in oxometal complexes without metal-ligand bond cleavage (twists) are known for molybdenum complexes that serve as synthetic models of molybdenum dependent oxotransferases[45–49] and in a $Re^{V}O$

© 2022 The Authors. Angewandte Chemie International Edition published by Wiley-VCH GmbH

15213773, 2023, 2, Downloaded from https://onlinelibrary.wiley.com/doi/10.1002/anie.202211361 by Universidad De Cadiz, Wiley Online Library on [28/09/2023]. See the Terms and Conditions (https://onlinelibrary.wiley.com/terms-and-conditions) on Wiley Online Library for rules of use; OA articles are governed by the applicable Creative Commons License

complex.[50] On the other hand, dissociative mechanisms are rarer, and are exemplified by *cis/trans*-$Re^{V}O(CH_3)_2Cl$-(bpy),[51] and more recently in a molybdenum(IV) oxido isocyanide complex.[52] However, isomerization of the oxo ligand to a *cis* site has not been described yet for iron complexes. Previously described examples exclusively detail isomerizations towards *trans* sites on the basis of an oxo-hydroxo tautomerism.[36,53–55]

The Kinetics of Hydrogen Atom Transfer (HAT)

The kinetics of HAT processes was studied for the reaction of ^{R}**2a** and ^{R}**2b** with 1,4-cyclohexadiene (CHD) and 9,10-dihydroanthracene (DHA). Fitting of the UV/Vis spectral changes for the reaction of the mixture of isomers formed at short reaction times requires a kinetic model with two steps, and global analysis of the data indicate that the first step corresponds to the reaction of isomer ^{R}**2a** whereas the second one corresponds to isomer ^{R}**2b**. However, the values of the rate constants for ^{R}**2b** were better estimated from sequential-mixing experiments in which the substrate is added once isomerization is complete, for which the spectral changes could be satisfactorily fitted by a single kinetic step, and so these are the reported values. In all cases, a linear dependence of the rate constants with the substrate concentration was observed for both isomers (Figures S99, S102, S105, S108, S111, S114, S122). In some cases, the plots show a non-zero intercept which can be assigned to isomerization in the case of ^{R}**2a** and to self-decay in the case of ^{R}**2b**. As these intercepts are negligible in most cases, they were not investigated in detail, and the discussion below is based on the second order rate constants derived from the slopes in the plots. The main oxidation products derived from these reactions correspond to anthracene and benzene for DHA and CHD, respectively, in almost quantitative yields as determined for ^{H}**2b** (Table S34).

Tables 2 and S32 summarize the kinetic results for HAT reactions, and they show that the reaction of both isomers with DHA is in general slightly faster but the rate constants never differ by a factor larger than three with respect to CHD. For both substrates ^{R}**2a** reacts about one order of magnitude faster than ^{R}**2b**, with k_{2a}/k_{2b} values within the 13–32 range for the whole set of experiments with CHD and DHA. Interestingly, the nature of the substituent in the *para*-position of the pyridine ring does not significantly affect reaction rates (see below). Regarding the KIE value for the reaction with DHA (see Section 6.2 in the Supporting Information), the most important observation is the existence of a significant KIE for both isomers (Table S32), the values for ^{R}**2a** (range: 12–22) being in most cases slightly larger than those for ^{R}**2b** (range: 7.3–20), although the differences are probably not very significant. All values for both isomers are somewhat larger than those expected from a classical model and suggest contributions from tunneling.[56,57]

Computational Analysis of the HAT Reactions

DFT calculations were performed to shed some light in the origin of the faster reactivity of ^{R}**2a** with respect to ^{R}**2b**. In particular, we computed the activation barriers for the HAT reaction with CHD as substrate for both ^{H}**2a** and ^{H}**2b**. The reaction Gibbs energy profile was computed for both S = 1 and S = 2 spin states (Figure 6a). For species **I** and **II**, the predicted relative stability of S = 1 and S = 2 states depends on the chosen functional (the ground states are S = 2 for M06 L, whereas they are S = 1 for ωB97XD), as both spin states are close in energy. However, **TS(II–III)** and **III** are clearly better described as S = 2 compounds by all the DFT methods tested. The reaction Gibbs energy profile starts with the formation of the reactant complex, which is endergonic due to the entropy contribution, indicating that the reactant complex is not stable. In the following step, the HAT transition state is reached, **TS(II–III)**, which is 1.6 kcal mol^{-1} lower in energy for ^{H}**2a** than for ^{H}**2b**, which is in agreement with the relative values of the experimental rate constants, indicating that HAT is the rate-determining step of the reaction. In all the HAT transition states the substrate approaches sideways (TS Fe–O–H angles for ^{H}**2a** and ^{H}**2b** are 125° and 138° respectively), thus the reaction proceeds via π-channel, i.e. through the π_{xy}* Fe–O molecular orbital (Figure 6b).[58–60] We also tried to optimize the σ-

Table 2: Summary of kinetic data and activation parameters for the reaction of ^{R}**2a** and ^{R}**2b** with CHD in acetonitrile solution.

R	^{R}**2a**					^{R}**2b**					k_{2a}/k_{2b}
	k_{2a} at −35 °C [M^{-1} s^{-1}]	$\Delta H^{\neq}$ [kcal mol^{-1}]	$\Delta S^{\neq}$ [cal K^{-1} mol^{-1}]	$\Delta G_{243}{}^{\neq}$[a] [kcal mol^{-1}]	$\Delta G_{243}{}^{\neq}$[b] [kcal mol^{-1}]	k_{2b} at −35 °C [M^{-1} s^{-1}]	$\Delta H^{\neq}$ [kcal mol^{-1}]	$\Delta S^{\neq}$ [cal K^{-1} mol^{-1}]	$\Delta G_{243}{}^{\neq}$[a] [kcal mol^{-1}]	$\Delta G_{243}{}^{\neq}$[b] [kcal mol^{-1}]	
OMe	41.0(9)	7.1(6)	−21(3)	12.14(2)	12.19	2.5(2)	5.1(5)	−35(2)	13.52(2)	13.51	16(1)
H	38(1)	7.4(6)	−20(2)	12.16(2)	12.18	2.34(3)	3.4(4)	−42(1)	13.62(1)	13.65	16.2(5)
Cl	56(1)	9.1(7)	−12(3)	11.99(2)	12.03	2.50(8)	6.2(9)	−31(4)	13.63(2)	13.69	22.4(8)
Br	52(2)	3.8(4)	−34(2)	12.13(1)	12.17	2.5(1)	6.5(6)	−29(2)	13.57(2)	13.58	21(1)
CF_3	49(2)	4.4(2)	−32(1)	12.16(1)	12.17	2.75(2)	5.9(2)	−31(1)	13.50(1)	13.52	17.8(7)
CO_2Me	39.4(7)	8.7(6)	−14(3)	12.16(1)	12.17	3.0(2)	6.8(6)	−28(2)	13.49(1)	13.51	13.1(9)

[a] Results obtained by fitting to the Arrhenius equation at the mean harmonic temperature (T_{hm} = 243 K). [b] Value derived from the rate constant at −30 °C. The estimation of the errors is in all cases smaller than 0.01. Note that T_{hm} (harmonic mean) is slightly lower than the mean temperature (242.95 K vs. 243.15 K).

© 2022 The Authors. Angewandte Chemie International Edition published by Wiley-VCH GmbH

15213773, 2023, 2, Downloaded from https://onlinelibrary.wiley.com/doi/10.1002/anie.202211361 by Universidad De Cadiz, Wiley Online Library on [28/09/2023]. See the Terms and Conditions (https://onlinelibrary.wiley.com/terms-and-conditions) on Wiley Online Library for rules of use; OA articles are governed by the applicable Creative Commons License

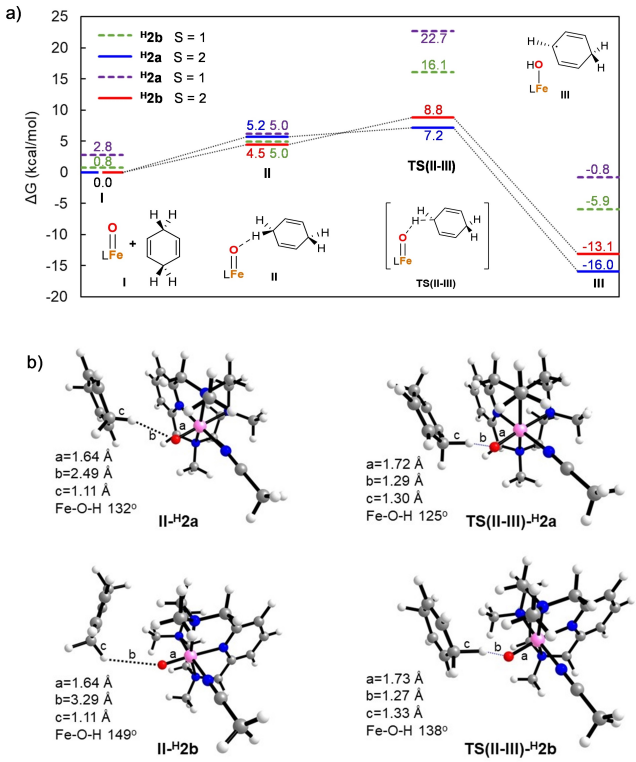

Figure 6. a) DFT Gibbs energy profile of the HAT reaction with CHD computed at UM06L-D3/Def2TZVP/SMD//UM06L-D3/Def2SVP/SMD level of theory for ^{H}**2a** S = 1 (purple), ^{H}**2a** S = 2 (blue), ^{H}**2b** S = 1 (green) and ^{H}**2b** S = 2 (red). b) Relevant geometrical parameters of the ground states of **II-**^{H}**2** and **TS$_{(II–III)}$**–^{H}**2**.

channel transition states, but all optimizations led to the angular π-channel HAT TS.

In order to understand the origin of the differences on the HAT chemical barrier of the two isomers, we thoroughly compared the key geometrical parameters of **II-**^{H}**2a** (**TS$_{(II-III)}$**–^{H}**2a**) and **II-**^{H}**2b** (**TS$_{(II–III)}$**–^{H}**2b**) involved in the reaction, namely the Fe-oxo, the oxo-H and the H–C(substrate) distances. For **II-**^{H}**2** the only substantial difference observed is the oxo-H distance that increases from 2.49 Å in **II-**^{H}**2a** to 3.29 Å in **II-**^{H}**2b**, suggesting that the steric repulsion is larger in the latter. To confirm this hypothesis, the noncovalent interactions that arise between the CHD and the $PyNMe_3$ ligand were analyzed using the NCIPLOT program,[61,62] which enables the identification of attractive and repulsive noncovalent interactions based on the real-space analysis of the reduced density gradient (Figure 7). Specifically, in ^{H}**2a**, the CHD substrate is located parallel to the pyridine ligand and there is a weakly-favorable interaction between them (green NCI surface) promoted by a π_{CHD}-π_{pyr} interaction that facilitates the approach of the substrate to the oxoiron moiety. On the contrary, in ^{H}**2b** there is a repulsive noncovalent interaction between a methyl group of the ligand and the CHD due to the steric clash between them that hampers the approach of the substrate to the oxoiron moiety. This steric repulsion in **II-**^{H}**2b** is the origin of the increase of its HAT activation barrier with respect to ^{H}**2a**. The analysis of the geometrical parameters of **TS$_{(II–III)}$**–^{H}**2**

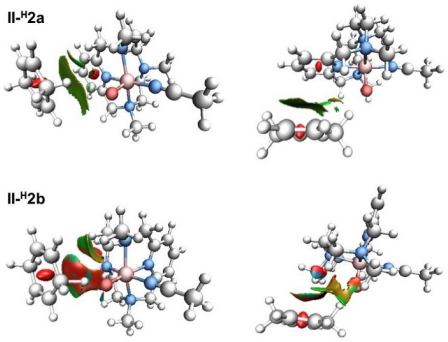

Figure 7. Noncovalent interactions isosurfaces generated by NCIPLOT (front and top views) for **II-**^{H}**2a** and **II-**^{H}**2b**. Green surfaces indicate weak favorable interactions, while red surfaces indicate steric clashes. The intra-complex NCI surfaces have been removed for clarity.

also show that, in complete agreement with the Hammond-Leffler postulate,[63,64] ^{H}**2a** presents an earlier **TS$_{(II-III)}$** than ^{H}**2b**. In this particular case, the electronic effects play a secondary role as **TS$_{(II–III)}$**–^{H}**2a** and **TS$_{(II–III)}$**–^{H}**2b** have very similar electronic structures (Figure S126).

Temperature Dependence and Hammett Plots of the HAT Reaction Rates

The temperature dependence of the rate constants for the reaction of ^{R}**2** with CHD was analyzed in the same way as the isomerization process, and similar comments could be made in this case (detailed Hammett, $\Delta H^{\neq}$ vs. $\Delta S^{\neq}$, and log *k* vs. *T* plots are included in the Supporting Information). Nevertheless, an important comment must be made at this point, as the data (Figure 8) show that the order of the rate constants for the compounds with the different R substituents is strongly temperature dependent, so that the ordering is $CO_2Me < H < MeO < Cl \approx CF_3 < Br$ at −40 °C, and Br ≈

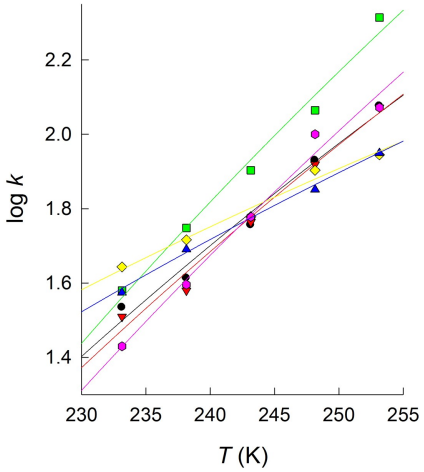

Figure 8. Plots of log *k* vs. *T* for the reaction of ^{R}**2a** with CHD in acetonitrile. R = MeO (black), H (red), Cl (green), Br (yellow), CO_2Me (pink) and CF_3 (blue).

© 2022 The Authors. Angewandte Chemie International Edition published by Wiley-VCH GmbH

15213773, 2023, 2, Downloaded from https://onlinelibrary.wiley.com/doi/10.1002/anie.202211361 by Universidad De Cadiz, Wiley Online Library on [28/09/2023]. See the Terms and Conditions (https://onlinelibrary.wiley.com/terms-and-conditions) on Wiley Online Library for rules of use; OA articles are governed by the applicable Creative Commons License

$CF_3 < CO_2Me \approx H < Cl$ at −20 °C for ^{R}**2a**. Thus, quite different conclusions could be derived on the effect of the substituents, thus showing the limitations of kinetic studies at a single temperature.

In contrast, Hammett plots clearly show that the nature of the substituent does not have any significant effect on the kinetics of hydrogen atom transfer. Thus, Figure 9 shows in all cases a slope close to zero. Of notice, the same trend is observed for the two different substrates and, as expected from the close energy of the C–H bonds in CHD and DHA, the plots for both substrates also show close mean values (Table S29).

The lack of impact of the electronic tuning of the $PyNMe_3$ family of oxoiron(IV) complexes in their HAT reactions was unexpected as it was envisioned that enhancing the electrophilicity of the hydrogen abstracting species (oxoiron(IV)) would facilitate the reactions,[65] which should be understood as oxidation processes. Ground state and transition state energetics should be considered to explain the data but it must be kept in mind that HAT reactions by high valent oxometal species frequently display linear free energy correlations that suggest concerted electron and proton transfer.[66] A thermodynamic cycle permits to divide the thermodynamic driving force of HAT in two components; an electrophilicity driving force, arising from the redox potential of the $M^{n+1}(O)/M^{n+}(O)$ couple and a basicity driving force arising from the $M^{n+1}(O)/M^{n+1}(OH)$ pair. Simple considerations regarding electron density at the metal predict that the two effects must respond in opposite directions as the oxometal unit is made more electron-poor, which can be viewed as a thermodynamic compensation.[67] Electrophilicity must obviously increase on going from complexes with electron-rich ligands to electron-poor ones. On the contrary, the basicity of the oxometal unit must decrease. The similarity in the HAT reaction rates among the series of electronically tuned complexes ^{R}**2** strongly indicates that the two factors are compensated in terms of thermodynamic free energy.

On the other hand, the lack of electronic effects in reaction rates is also informative about the transition states involved. In the frame of proton coupled electron transfer (PCET), HAT is generally described as the concerted transfer of a proton and an electron from one group to another in a single kinetic step.[66] In this case, a certain degree of asynchronicity in the proton and electron transfer may exist, so that proton or electron transfer may exhibit a more dominant role and some charge should accumulate in the substrate during the TS. However, this is not always the case. Indeed, recent work by Borovik and Green[68] suggests that oxometal systems exhibiting a strong correlation between $\log(k)$ and BDE_{C-H} follow synchronous HAT processes. In the same work, they provide an example in which there is no such correlation and the Hammett analysis shows a strong correlation with the σ_p values for the substituents in the substrate with a positive slope that supports an asynchronous PCET. In addition, Srnec and co-workers disclosed that those oxoiron species favoring dissociation over rebound mechanisms after HAT consistently show low degrees of asynchronicity.[69] Compound ^{R}**2** complies with these two requisites (correlation of reaction rates with C–H bond strength and a preference for dissociation over rebound mechanisms),[29] thus supporting the idea that its HAT reactivity is synchronous. We infer that the necessary consequence of this scenario is that positive charge is not effectively built up in the TS of hydrogen atom transfer in ^{R}**2**. The zero slope in the Hammett plot observed for the HAT reactions of the ^{R}**2a** and ^{R}**2b** series of complexes may reflect this situation.

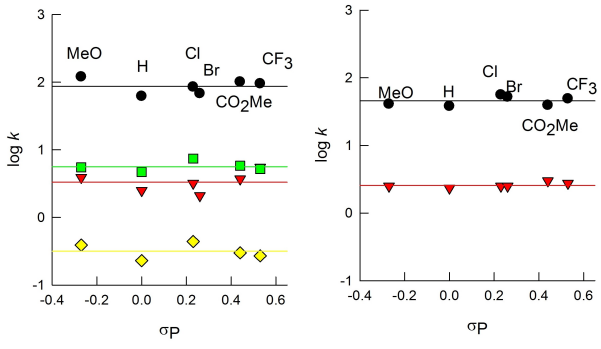

Figure 9. Hammett plots for the reaction of ^{R}**2** with DHA (left) and CHD (right) in acetonitrile at −35 °C: ^{R}**2a** (black) and ^{R}**2b** (red). The symbols and lines for the reaction with DHA-d_4 are shown in green (^{R}**2a**) and yellow (^{R}**2b**).

Computational Analysis of the Asynchronicity of the HAT

We have used the asynchronicity factor η defined by Srnec and co-workers that measures the degree of asynchronicity of H^+/e^- transfers in HAT in terms of the DFT reduction potentials and acidity constants of the reacting complex-substrate pair.[70] The η values for ^{R}**2a** and ^{R}**2b** are η = 506 mV and η = 471 mV, respectively, which indicate that both compounds operate through a quite synchronous HAT mechanism (see Supporting Information for further details).

The proposal that the synchronicity of the HAT is the origin of the lack of a Hammett slope is further supported by the different effects observed in the OAT reactions (vide infra), where charge accumulation in the substrate during the OAT results in reactions that are accelerated when the oxometal is made more electrophilic, and slowed down for less electrophilic oxidants.

The Kinetics of Oxygen Atom Transfer (OAT)

The effect of the R substituent on the kinetics of OAT processes for ^{R}**2** was studied using thioanisole as substrate (see section 7 in the Supporting Information for more details). The rate constants derived for both isomers are quite close to each other, ^{R}**2b** reacting slightly faster than ^{R}**2a** (Table S37). The k_{2a}/k_{2b} quotients are in the range 0.56–1.04, which indicates that the rate of reaction of both isomers never differ by more than a factor of 2, which contrasts with the results obtained for HAT processes, in

© 2022 The Authors. Angewandte Chemie International Edition published by Wiley-VCH GmbH

15213773, 2023, 2, Downloaded from https://onlinelibrary.wiley.com/doi/10.1002/anie.202211361 by Universidad De Cadiz, Wiley Online Library on [28/09/2023]. See the Terms and Conditions (https://onlinelibrary.wiley.com/terms-and-conditions) on Wiley Online Library for rules of use; OA articles are governed by the applicable Creative Commons License

which ^{R}**2a** reacts much faster. The values of $\Delta G_{238}^{\neq}$ in Table S37 were estimated directly from the rate constants, and they indicate that for a given R the $\Delta G_{2a}^{\neq}$ - $\Delta G_{2b}^{\neq}$ difference is quite small (<0.3 kcal mol^{-1}). For a given isomer the values of $\Delta G^{\neq}$ roughly decrease as the σ_P value of the R substituent increases. Actually, the Hammett plots (Figure 10) show a positive slope of 0.8(2) for ^{R}**2a** and 0.63(9) for ^{R}**2b**, which indicate that the oxygen atom transfer occurs through an electrophilic attack of the oxoiron(IV) intermediates to the substrate. The observed positive slope in the Hammett plot was also rationalized by DFT calculations, which confirmed the accumulation of negative charge (−0.52 electrons for both ^{H}**2a** and ^{H}**2b** isomers, Table S39) in the transition states of OAT processes, in line with previously studied sulfoxidation reactions performed by oxoiron(IV) complexes.[71]

Conclusion

In this work, a new family of oxoiron(IV) species (^{R}**2**) containing ^{R}PyNMe$_3$ ligands (R = OMe, Br, Cl, CO_2Me, CF_3) with systematically modulated electronic properties has been described. The ^{R}**2** complexes are initially formed as a mixture of two isomers that differ in the relative position of the oxo group in the iron coordination sphere, but the mixture evolves to complete formation of the thermodynamically favored isomer. Kinetic studies and DFT calculations lead to a mechanistic proposal for the isomerization process that involves a dissociative interchange mechanism. The mechanism constitutes a model to explain the "ferryl flip" postulated in several nonheme iron dependent oxygenases.[5,6] Kinetic studies show that the *para* substitution on the pyridine ring of the ligand has no influence in HAT reactions and a small effect in OAT processes. Of particular relevance is the absence of slope in the Hammett plots for HAT processes, which can be interpreted in terms of synchronous PCET. Interestingly, the position of the oxo ligand in the coordination sphere of the iron(IV) center has an important effect in HAT processes. In contrast, the relative reactivity of the two isomers is virtually the same in OAT. An important new knowledge derived from the present kinetic results is that Hammett analysis is superior to the analysis of Eyring-derived activation parameters for assessing electronic effects on the reaction mechanism.

In summary, the work provides an unprecedented model to understand the "ferryl flip" postulated in several non-heme iron dependent oxygenases. It also illustrates that the position of the oxo ligand in the coordination sphere of the oxoiron center may have a larger effect on the C-H oxidation activity than the relative electrophilic character of the oxidant. On the other hand, systematic alteration of the electronic properties of the oxoiron(IV) provides insight about the nature of the HAT reaction. Specifically, the resulting Hammett analysis, denoting a practically flat correlation between HAT reaction rates and Hammett parameters, is in stark contrast with typical negative slopes of oxo transfer reactions, providing strong indication that the reaction takes place via a nearly synchronous PCET.

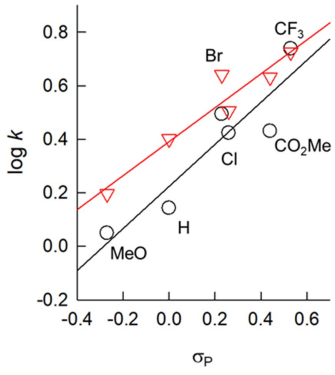

Figure 10. Hammett plot for the reaction of ^{R}**2a** (black) and ^{R}**2b** (red) with thioanisole in acetonitrile solution at −35 °C.

Acknowledgements

The authors thank the Spanish Ministry of Science (PID2019-106699GB-I00 to A.C., PID2019-107006GB-C22 to M. G.-B., PID2019-110751RB-I00 to E.G.-E., CEX2019-000919-M to E.G.-E. and PGC2018-098212-B-C22 to J.M.L.) and Generalitat de Catalunya (ICREA Academia Award and 2017SGR264 project to M.C. and A.C.; 2017SGR39 project to J.M.L.) for financial support. The Spanish Ministry of Science is acknowledged for a M. Zambrano contract to E. D.-P. and for the FPU17/02058 grant to P.B.-S. M.C.P.-S. acknowledges a FPI-UCA grant from Universidad de Cádiz. A. M.-C. thanks Generalitat Valenciana and the ESF for the postdoc grant APOSTD/2020/065. P.B.-S and J.M.L are grateful for computational time financed by CSUC. Support from the Mass Spectrometry and NMR service of the SCSIE at the University of Valencia is also acknowledged.

Conflict of Interest

The authors declare no conflict of interest.

Data Availability Statement

The data that support the findings of this study are available in the supplementary material of this article.

Keywords: Atom Transfer · Iron · Isomerization · Oxidation · Oxoiron

[1] J. C. Price, E. W. Barr, B. Tirupati, J. M. Bollinger Jr., C. Krebs, *Biochemistry* **2003**, *42*, 7497–7508.
[2] M. Costas, M. P. Mehn, M. P. Jensen, L. Que Jr., *Chem. Rev.* **2004**, *104*, 939–986.
[3] P. C. A. Bruijnincx, G. van Koten, R. J. M. Klein Gebbink, *Chem. Soc. Rev.* **2008**, *37*, 2716–2744.

© 2022 The Authors. Angewandte Chemie International Edition published by Wiley-VCH GmbH

15213773, 2023, 2, Downloaded from https://onlinelibrary.wiley.com/doi/10.1002/anie.202211361 by Universidad De Cadiz, Wiley Online Library on [28/09/2023]. See the Terms and Conditions (https://onlinelibrary.wiley.com/terms-and-conditions) on Wiley Online Library for rules of use; OA articles are governed by the applicable Creative Commons License

[4] T. L. Poulos, *Chem. Rev.* **2014**, *114*, 3919–3962.
[5] Z. Zhang, J.-S. Ren, K. Harlos, C. H. McKinnon, I. J. Clifton, C. J. Schofield, *FEBS Lett.* **2002**, *517*, 7–12.
[6] S. O. Waheed, R. Ramanan, S. S. Chaturvedi, N. Lehnert, C. J. Schofield, C. Z. Christov, T. G. Karabencheva-Christova, *ACS Cent. Sci.* **2020**, *6*, 795–814.
[7] D. P. Galonić, E. W. Barr, C. T. Walsh, J. M. Bollinger Jr., C. Krebs, *Nat. Chem. Biol.* **2007**, *3*, 113–116.
[8] M. L. Matthews, C. M. Krest, E. W. Barr, F. H. Vaillancourt, C. T. Walsh, M. T. Green, C. Krebs, J. M. Bollinger Jr., *Biochemistry* **2009**, *48*, 4331–4343.
[9] T. Borowski, H. Noack, M. Radoń, K. Zych, P. E. M. Siegbahn, *J. Am. Chem. Soc.* **2010**, *132*, 12887–12898.
[10] A. R. McDonald, L. Que Jr., *Coord. Chem. Rev.* **2013**, *257*, 414–428.
[11] J. E. M. N. Klein, L. Que Jr., in *Encyclopedia of Inorganic and Bioinorganic Chemistry*, Wiley, Hoboken, **2011**, pp. 1–22.
[12] M. Guo, T. Corona, K. Ray, W. Nam, *ACS Cent. Sci.* **2019**, *5*, 13–28.
[13] M. Puri, L. Que Jr., *Acc. Chem. Res.* **2015**, *48*, 2443–2452.
[14] J. L. Lee, D. L. Ross, S. K. Barman, J. W. Ziller, A. S. Borovik, *Inorg. Chem.* **2021**, *60*, 13759–13783.
[15] A. E. Anastasi, P. Comba, J. McGrady, A. Lienke, H. Rohwer, *Inorg. Chem.* **2007**, *46*, 6420–6426.
[16] J. Prakash, G. T. Rohde, K. K. Meier, E. Münck, L. Que Jr., *Inorg. Chem.* **2015**, *54*, 11055–11057.
[17] A. Company, I. Prat, J. R. Frisch, D. R. Mas-Ballesté, M. Güell, G. Juhász, X. Ribas, D. E. Münck, J. M. Luis, L. Que Jr., M. Costas, *Chem. Eur. J.* **2011**, *17*, 1622–1634.
[18] E. Andris, K. Segers, J. Mehara, L. Rulíšek, J. Roithová, *Angew. Chem. Int. Ed.* **2020**, *59*, 23137–23144; *Angew. Chem.* **2020**, *132*, 23337–23344.
[19] R. Singh, G. Ganguly, S. O. Malinkin, S. Demeshko, F. Meyer, E. Nordlander, T. K. Paine, *Inorg. Chem.* **2019**, *58*, 1862–1876.
[20] G. Mukherjee, A. Alili, P. Barman, D. Kumar, C. V. Sastri, S. P. de Visser, *Chem. Eur. J.* **2019**, *25*, 5086–5098.
[21] T. K. Paine, M. Costas, J. Kaizer, L. Que Jr., *J. Biol. Inorg. Chem.* **2006**, *11*, 272–276.
[22] W. Rasheed, A. Draksharapu, S. Banerjee, V. G. Young Jr, R. Fan, Y. Guo, M. Ozerov, J. Nehrkorn, J. Krzystek, J. Telser, L. Que Jr., *Angew. Chem. Int. Ed.* **2018**, *57*, 9387–9391; *Angew. Chem.* **2018**, *130*, 9531–9535.
[23] C. V. Sastri, J. Lee, K. Oh, Y. J. Lee, J. Lee, T. A. Jackson, K. Ray, H. Hirao, W. Shin, J. A. Halfen, J. Kim, L. Que Jr., S. Shaik, W. Nam, *Proc. Natl. Acad. Sci. USA* **2007**, *104*, 19181–19186.
[24] I. Monte Pérez, X. Engelmann, Y.-M. Lee, M. Yoo, E. Kumaran, E. R. Farquhar, E. Bill, J. England, W. Nam, M. Swart, K. Ray, *Angew. Chem. Int. Ed.* **2017**, *56*, 14384–14388; *Angew. Chem.* **2017**, *129*, 14576–14580.
[25] P. Comba, D. Faltermeier, S. Krieg, B. Martin, G. Rajaraman, *Dalton Trans.* **2020**, *49*, 2888–2894.
[26] D. Wang, K. Ray, M. J. Collins, E. R. Farquhar, J. R. Frisch, L. Gómez, T. A. Jackson, M. Kerscher, A. Waleska, P. Comba, M. Costas, L. Que Jr., *Chem. Sci.* **2013**, *4*, 282–291.
[27] Y. Zhou, X. Shan, R. Mas-Ballesté, M. R. Bukowski, A. Stubna, M. Chakrabarti, L. Slominski, J. A. Halfen, E. Münck, L. Que Jr., *Angew. Chem. Int. Ed.* **2008**, *47*, 1896–1899; *Angew. Chem.* **2008**, *120*, 1922–1925.
[28] T. Chantarojsiri, Y. Sun, J. R. Long, C. J. Chang, *Inorg. Chem.* **2015**, *54*, 5879–5887.
[29] V. Dantignana, J. Serrano-Plana, A. Draksharapu, C. Magallón, S. Banerjee, R. Fan, I. Gamba, Y. Guo, L. Que Jr., M. Costas, A. Company, *J. Am. Chem. Soc.* **2019**, *141*, 15078–15091.
[30] J. Serrano-Plana, W. N. Oloo, L. Acosta-Rueda, K. K. Meier, B. Verdejo, E. García-España, M. G. Basallote, E. Münck, L. Que Jr., A. Company, M. Costas, *J. Am. Chem. Soc.* **2015**, *137*, 15833–15842.
[31] R. Fan, J. Serrano-Plana, W. N. Oloo, A. Draksharapu, E. Delgado-Pinar, A. Company, V. Martin-Diaconescu, M. Borrell, J. Lloret-Fillol, E. García-España, Y. Guo, E. L. Bominaar, L. Que Jr., M. Costas, E. Münck, *J. Am. Chem. Soc.* **2018**, *140*, 3916–3928.
[32] Deposition numbers 2192962, 2192963, 2192964 and 2192965 contain the supplementary crystallographic data for this paper. These data are provided free of charge by the joint Cambridge Crystallographic Data Centre and Fachinformationszentrum Karlsruhe Access Structures service.
[33] I. Prat, A. Company, T. Corona, T. Parella, X. Ribas, M. Costas, *Inorg. Chem.* **2013**, *52*, 9229–9244.
[34] G. J. P. Britovsek, J. England, A. J. P. White, *Inorg. Chem.* **2005**, *44*, 8125–8134.
[35] M. A. Mekhail, K. Pota, T. M. Schwartz, K. N. Green, *RSC Adv.* **2020**, *10*, 31165–31170.
[36] J. Prakash, Y. Sheng, A. Draksharapu, J. E. M. N. Klein, C. J. Cramer, L. Que Jr., *Angew. Chem. Int. Ed.* **2019**, *58*, 1995–1999; *Angew. Chem.* **2019**, *131*, 2017–2021.
[37] J. Bernadou, B. Meunier, *Chem. Commun.* **1998**, 2167–2173.
[38] M. S. Seo, J.-H. In, S. O. Kim, N. Y. Oh, J. Hong, J. Kim, L. Que Jr., W. Nam, *Angew. Chem. Int. Ed.* **2004**, *43*, 2417–2420; *Angew. Chem.* **2004**, *116*, 2471–2474.
[39] L. Helm, A. E. Merbach, *Chem. Rev.* **2005**, *105*, 1923–1960.
[40] H. Erras-Hanauer, T. Clark, R. van Eldik, *Coord. Chem. Rev.* **2003**, *238–239*, 233–253.
[41] E. Ramos-Cordoba, V. Postils, P. Salvador, *J. Chem. Theory Comput.* **2015**, *11*, 1501–1508.
[42] a) V. Postils, C. Delgado-Alonso, J. M. Luis, P. Salvador, *Angew. Chem. Int. Ed.* **2018**, *57*, 10525–10529; b) E. Ramos-Cordoba, P. Salvador, I. Mayer, *J. Chem. Phys.* **2013**, *138*, 214107.
[43] F. Riblet, G. Novitchi, R. Scopelliti, L. Helm, A. Gulea, A. E. Merbach, *Inorg. Chem.* **2010**, *49*, 4194–4211.
[44] A. Gavriluta, G. E. Büchel, L. Freitag, G. Novitchi, J. B. Tommasino, E. Jeanneau, P.-S. Kuhn, L. González, V. B. Arion, D. Luneau, *Inorg. Chem.* **2013**, *52*, 6260–6272.
[45] K. Heinze, *Coord. Chem. Rev.* **2015**, *300*, 121–141.
[46] J. T. Hoffman, S. Einwaechter, B. S. Chohan, P. Basu, C. J. Carrano, *Inorg. Chem.* **2004**, *43*, 7573–7575.
[47] B. Kail, V. N. Nemykin, S. R. Davie, C. J. Carrano, B. Hammes, P. Basu, *Inorg. Chem.* **2002**, *41*, 1281–1291.
[48] B. W. Kail, P. Basu, *Dalton Trans.* **2006**, 1419–1423.
[49] J. T. Hoffman, B. L. Tran, C. J. Carrano, *Dalton Trans.* **2006**, 3822–3830.
[50] D. W. Lahti, J. H. Espenson, *J. Am. Chem. Soc.* **2001**, *123*, 6014–6024.
[51] J.-H. Jung, T. A. Albright, D. M. Hoffman, T. Randall Lee, *J. Chem. Soc. Dalton Trans.* **1999**, 4487–4494.
[52] J. Leppin, C. Förster, K. Heinze, *Inorg. Chem.* **2014**, *53*, 1039–1047.
[53] J. E. M. N. Klein, A. Draksharapu, A. Shokri, C. J. Cramer, L. Que Jr., *Chem. Eur. J.* **2018**, *24*, 5373–5378.
[54] M. Puri, A. Company, G. Sabenya, M. Costas, L. Que Jr., *Inorg. Chem.* **2016**, *55*, 5818–5827.
[55] S. Schaub, A. Miska, J. Becker, S. Zahn, D. Mollenhauer, S. Sakshath, V. Schünemann, S. Schindler, *Angew. Chem. Int. Ed.* **2018**, *57*, 5355–5358; *Angew. Chem.* **2018**, *130*, 5453–5456.
[56] Z. Pan, J. H. Horner, M. Newcomb, *J. Am. Chem. Soc.* **2008**, *130*, 7776–7777.
[57] J. Kaizer, E. J. Klinker, N. Y. Oh, J.-U. Rohde, W. J. Song, A. Stubna, J. Kim, E. Münck, W. Nam, L. Que Jr., *J. Am. Chem. Soc.* **2004**, *126*, 472–473.
[58] S. P. de Visser, *J. Am. Chem. Soc.* **2010**, *132*, 1087–1097.

© 2022 The Authors. Angewandte Chemie International Edition published by Wiley-VCH GmbH

15213773, 2023, 2, Downloaded from https://onlinelibrary.wiley.com/doi/10.1002/anie.202211361 by Universidad De Cadiz, Wiley Online Library on [28/09/2023]. See the Terms and Conditions (https://onlinelibrary.wiley.com/terms-and-conditions) on Wiley Online Library for rules of use; OA articles are governed by the applicable Creative Commons License

[59] S. Ye, C.-Y. Geng, S. Shaik, F. Neese, *Phys. Chem. Chem. Phys.* **2013**, *15*, 8017–8030.
[60] A. Decker, J.-U. Rohde, E. J. Klinker, S. D. Wong, L. Que Jr., E. I. Solomon, *J. Am. Chem. Soc.* **2007**, *129*, 15983–15996.
[61] E. R. Johnson, S. Keinan, P. Mori-Sánchez, J. Contreras-García, A. J. Cohen, W. Yang, *J. Am. Chem. Soc.* **2010**, *132*, 6498–6506.
[62] J. Contreras-García, E. R. Johnson, S. Keinan, R. Chaudret, J.-P. Piquemal, D. N. Beratan, W. Yang, *J. Chem. Theory Comput.* **2011**, *7*, 625–632.
[63] G. S. Hammond, *J. Am. Chem. Soc.* **1955**, *77*, 334–338.
[64] J. E. Leffler, *Science* **1953**, *117*, 340–341.
[65] M. Bietti, *Angew. Chem. Int. Ed.* **2018**, *57*, 16618–16637; *Angew. Chem.* **2018**, *130*, 16858–16878.
[66] J. W. Darcy, B. Koronkiewicz, G. A. Parada, J. M. Mayer, *Acc. Chem. Res.* **2018**, *51*, 2391–2399.
[67] R. G. Agarwal, S. C. Coste, B. D. Groff, A. M. Heuer, H. Noh, G. A. Parada, C. F. Wise, E. M. Nichols, J. J. Warren, J. M. Mayer, *Chem. Rev.* **2022**, *122*, 1–49.
[68] S. K. Barman, M.-Y. Yang, T. H. Parsell, M. T. Green, A. S. Borovik, *Proc. Natl. Acad. Sci. USA* **2021**, *118*, e2108648118.
[69] M. Maldonado-Domínguez, M. Srnec, *J. Am. Chem. Soc.* **2020**, *142*, 3947–3958.
[70] D. Bím, M. Maldonado-Domínguez, L. Rulíšek, M. Srnec, *Proc. Natl. Acad. Sci. USA* **2018**, *115*, E10287–E10294.
[71] S. Kumar, A. S. Faponle, P. Barman, A. K. Vardhaman, C. V. Sastri, D. Kumar, S. P. de Visser, *J. Am. Chem. Soc.* **2014**, *136*, 17102–17115.

Manuscript received: August 2, 2022
Accepted manuscript online: October 28, 2022
Version of record online: December 2, 2022

© 2022 The Authors. Angewandte Chemie International Edition published by Wiley-VCH GmbH

15213773, 2023, 2, Downloaded from https://onlinelibrary.wiley.com/doi/10.1002/anie.202211361 by Universidad De Cadiz, Wiley Online Library on [28/09/2023]. See the Terms and Conditions (https://onlinelibrary.wiley.com/terms-and-conditions) on Wiley Online Library for rules of use; OA articles are governed by the applicable Creative Commons License